Internal Dynamics Interact with Proprioceptive Feedback During Movement Execution in an RNN Model of Motor Cortex

Hongru Jiang[a,1], Xiangdong Bu[a,1], Zhiyan Zheng[a], Xiaochuan Pan[b] and Yao Chen[a,*]

[a] School of Biomedical Engineering, Shanghai Jiao Tong University, Shanghai, 200240, China
[b] School of Mathematics, East China University of Science and Technology, Shanghai, 200237, China

ARTICLE INFO

Keywords:
Motor cortex
Proprioceptive feedback
Inhibitory stabilized network
Neural population dynamics
Movement Execution

ABSTRACT

The motor cortex initiates movement by sending temporal patterns to downstream neural circuitry. The patterns during movement execution are thought to arise from the internal dynamics within motor cortical network. However, external inputs such as proprioception also shape motor cortical dynamics. To investigate the contribution of internal dynamics and proprioceptive feedback to voluntary movement execution, we built several motor cortex models with different combinations of proprioceptive feedback to control artificial hand movements in the delayed reach task. We found that the inhibitory stabilized network receives hand kinematics and muscle force generated patterns most similar to those observed in motor cortex neuronal data. Furthermore, we used a disruption strategy to dissect the contribution of internal dynamics and proprioceptive feedback, and found that internal dynamics dominate, while proprioceptive feedback fine-tunes motor command. Ablation experiment demonstrates that proprioceptive feedback improves the robustness against noisy initial conditions. Finally, considering the delay, noise, and source of sensory feedback in the proprioceptive pathway, we constructed a sensory estimation network. Our results highlight the necessity of integrating intrinsic architecture and external input in motor control models, promoting the development of brain-inspired artificial intelligence systems.

1. Introduction

Voluntary movement, such as reaching, grasping, and speaking, is central to our interaction with the world. The motor cortex (MC), which orchestrates intricate neural pathways to generate motor command, is critical for planning and executing movement. Electrophysiological recordings in non-human primates have revealed that neuronal activity in the MC represents movement kinematics, including direction (Georgopoulos et al., 1982), velocity (Inoue et al., 2018) and isometric force (Sergio et al., 2005). However, this perspective only partially explains complex single-neuron multiphasic firing rate (Kalaska, 2019).

With advances in recording technologies and computational methods, the focus on MC has shifted from the representation of output to how motor command is created (Figure 1A). Firing rates of all neurons (neural population responses) in MC coordinate patterns for a particular movement. Recent studies have emphasized that MC is a dynamical system where future state depends on its current state and dynamical rule that dictates evolution (Churchland et al., 2012, 2010; Shenoy et al., 2013; Vyas et al., 2020). The dynamics result from the internal dynamics within MC (neuronal connectivity) and external inputs from other areas. Under the dynamical systems view, Churchland et al. (2012) projected population responses into low-dimensional space by their own dimensionality reduction method named jPCA and found rotational dynamics of the MC when monkeys perform reach task. Neural population responses in the state space from different starting point, follow rotational paths in the same direction for all movements. These rotational patterns revealed the simple nature of complex individual neural responses (Churchland et al., 2012). Furthermore, the dynamical system perspective has paved the way for interpreting motor cortical activity via recurrent neural networks (RNNs) — abstract neural computational of interconnected neurons. In one class of models, the MC is approximated as an autonomous dynamical system during movement execution, with negligible external input (Figure 1B) (Churchland et al., 2012; Hennequin et al., 2014; Sussillo et al., 2015; Zimnik and Churchland, 2021; Michaels et al., 2016). Neural population responses evolve from a specific initial condition, defined as the firing rates at movement onset (Afshar et al., 2011; Churchland et al., 2010), under the control of strong internal dynamics within MC. These models not only generate neural responses similar to real data at single-cell level, but also display rotational dynamics at population level (Churchland et al., 2012).

However, the impact of noise on movement execution in autonomous dynamical systems depends on the subspace in which the perturbations occur. Noise in subspaces orthogonal to the movement execution may not interfere with normal movement and can be readily corrected, while perturbations in the output direction can disrupt the intended movement, making the system sensitive to initial conditions in this subspace. However, the autonomous dynamical system is vulnerable to perturbations in output-relevant dimensions and unable to correct errors from an intended movement. The neural state at movement onset can only vary in a limited subspace, fail tolerate large neural variability.

Alternatively, there is a growing recognition of the role that external inputs play in shaping motor cortical activity (Figure 1C). Situated within a vast and distributed brain

**Corresponding author
yao.chen@sjtu.edu.cn (Y. Chen)
ORCID(s):

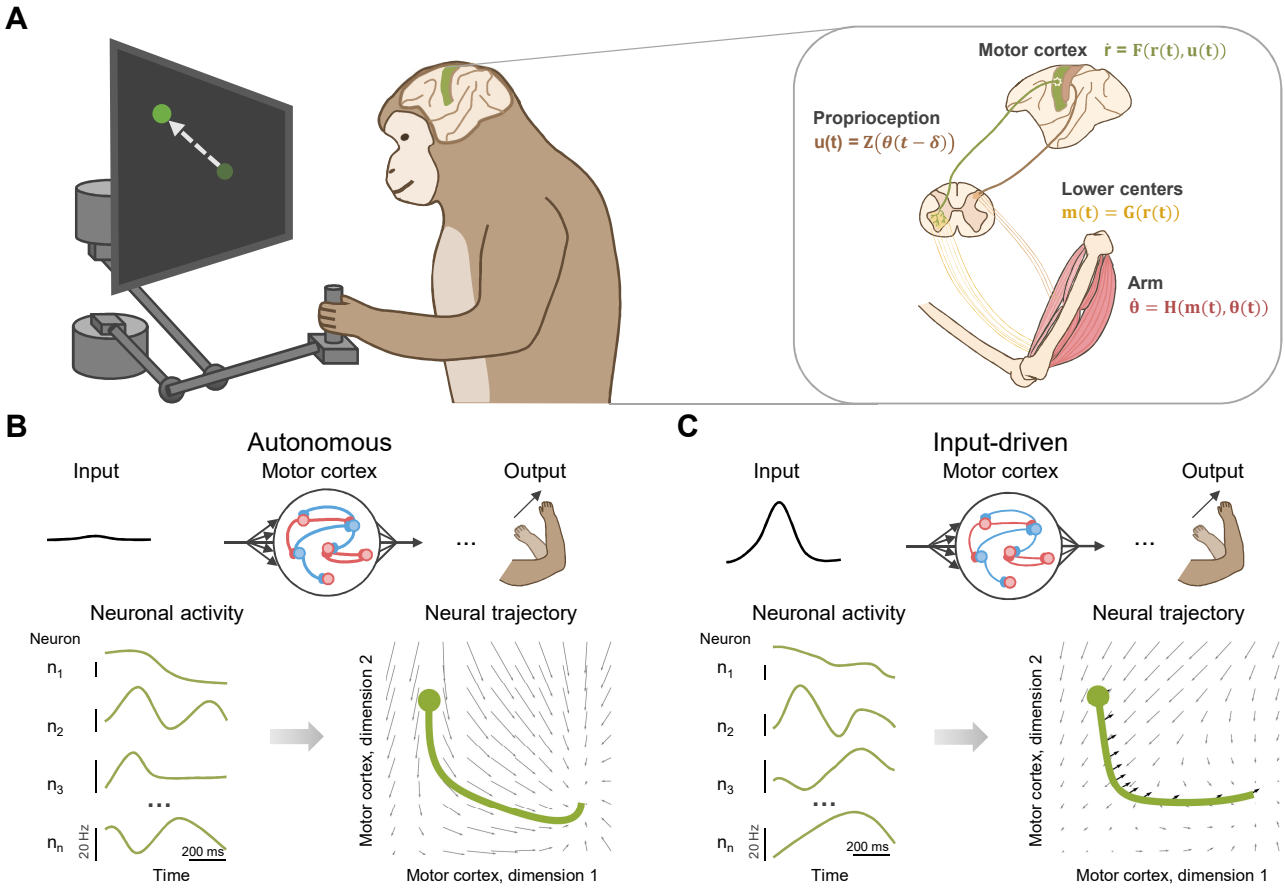

Figure 1: Motor cortex controls reaching under the perspective of dynamical system. (A) Dynamical system perspective on reaching movement. Left: illustration of the delayed reach task. A monkey puts its hand on a planar manipulandum to the center of the workspace to initiate the trial. After a randomized delay, a peripheral target appears, indicating the location the monkey is to reach. Monkey was trained to hold during a variable delay period until a go cue (e.g., auditory signal) prompts the monkey to reach the target. Right: dynamical system model of reaching. Motor cortical firing rates, evolving with a derivative $\dot{r}$, are determined by the internal dynamics in the MC and external input. Firing rates is converted into muscle activity $m(t)$ via a downstream circuit in lower motor centers, thereby updating the joint angles and velocities $\theta(t)$, ultimately reflected in hand movement. Delayed sensory feedback from the arm is sent back to the brain regions outside the MC. (B) MC as an autonomous dynamical system during movement execution. Neuronal population responses are visualized in a low-dimensional state-space, with neural states evolving from specific initial conditions (solid circle) under strong internal dynamics within the MC (grey arrows). The length of arrows illustrates the strength of dynamics. (C) MC as an input-driven dynamical system during movement execution. Neural firing rates starting from the initial condition, are driven by external input (black arrows) and internal dynamics (grey arrows). The internal dynamics are weaker than (C).

network, the MC integrates various external inputs, such as sensory feedback (Sauerbrei et al., 2020; Kalidindi et al., 2021; Gallego et al., 2020), thalamic (Sauerbrei et al., 2020; Logiaco et al., 2021; Yu et al., 2022) and cerebellar signals (Kumar and Ma, 2023). Sensory feedback is critical in finely controlled movements, as the MC has to integrate multiple sensory information including proprioception, vision and tactile sensation, to generate precise commands. The dynamical system perspective is also reflected in the framework of optimal feedback control (OFC), wherein the MC acts as a feedback controller using the best estimate of sensory feedback to produce motor output (Lillicrap and Scott, 2013; Omrani et al., 2017; Todorov and Jordan, 2002). OFC, which has successfully explained experimental behavior (Scott, 2004; Todorov and Jordan, 2002), is also expected to shape motor cortical dynamics during movement execution (Herter et al., 2009; Perich et al., 2020). A recent study found that sensory feedback also exhibits rotational dynamics, suggesting that sensory feedback may be determinant in cortical pattern generation (Kalidindi et al., 2021). Yet for the complete movement process, this model simplifies the external input as merely sensory information during preparatory period, potentially overstating the contribution of sensory feedback during movement execution.

Our study focuses on proprioceptive feedback, a critical component in motor control. The absence of proprioception leads to significant motor deficits, even when visual feedback is available (Sainburg et al., 1995). Healthy individuals estimate hand motion rely almost on proprioceptive feedback compared to visual feedback (Crevecoeur et al.,

2016). In this work, we investigate the interaction between proprioceptive feedback and internal dynamics in the MC during movement execution of delayed-reach task. Utilizing the inhibitory stabilized network (ISN) (Hennequin et al., 2014; Kao et al., 2021), we first built a baseline model that receives the feedback of hand kinematics and muscle force in a noise-free environment. Considering the MC generates motor command in the face of delayed and noisy feedback and receptors in the arm do not encode hand kinematics directly, we then built a sensory estimation network to estimate the proprioception. We incorporate the baseline and sensory estimation into a complete model, which generates firing rates that resembled real data at both single-cell and population levels, both qualitatively and quantitatively. We found the elaborate recurrent structure and proprioceptive feedback are important in motor cortical dynamics. Furthermore, we dissected their contribution by disrupting them at graded percentage of timecourse, and found the absence of internal dynamics causes neural activity out of control, whereas the absence of proprioceptive feedback led to ceaseless movement. These results suggest that internal dynamics are dominant in cortical pattern generation, while proprioceptive feedback is essential for speed control. Additionally, proprioceptive feedback tames sensitivity to initial conditions thus improves robustness of the network.

In summary, our research offers new insights into the intricate interaction between the internal dynamics within MC and proprioceptive feedback during movement execution, potentially reshaping our understanding of motor control.

2. Method

In this section, we elaborate the modeling framework and optimization, as well as the analysis of monkey and optimized model data.

2.1. Modeling framework

We construct our model in the framework of thalamocortical circuit model (Kao et al., 2021), controlling artificial hand movements. We first describe the overall model architecture, and then specified each building block including the MC model, musculoskeletal arm model. Additionally, we illustrate proprioceptive input and initial condition setup.

2.1.1. Model architecture

The gated thalamocortical circuit model enables fast preparation and explains the observed orthogonality between preparatory and movement neural activity (Kao et al., 2021) (Figure 2). The simulation was divided into two epochs by the gated action of basal ganglia: the preparation-epoch (before go cue) where basal ganglia disinhibited thalamic neurons, leaving them to interact with cortex. The execution-epoch (after go cue) where basal ganglia inhibited thalamic neurons and opened the loop. Furthermore, several constraints were implemented to ensure both biological plausibility and computational feasibility: (1) the MC was divided into the MC and the MC layer 4, and all the connection in the circuit satisfied Dale law. (2) integration dynamics in the thalamus and the MC layer 4 is omitted. (3) muscle activity was artificially set to 0 during movement preparation, bypassing spinal cord modeling for posture control. The corresponding dynamics of our circuit model can be described as:

$$\begin{aligned} \tau\frac{d\boldsymbol{x}}{dt} &= -\boldsymbol{x}(t) + \boldsymbol{W}\,[\boldsymbol{x}(t)]^{+} + \boldsymbol{\zeta}(t) + \boldsymbol{u}^{*} + \boldsymbol{u}^{t} + \boldsymbol{K}_{xz}\,[\boldsymbol{z}(t)]^{+} \\ \frac{d\boldsymbol{z}}{dt} &= -\boldsymbol{z} + \boldsymbol{K}_{zy}\,[\boldsymbol{y}(t)]^{+} \\ \frac{d\boldsymbol{y}}{dt} &= -\boldsymbol{y} + \boldsymbol{K}_{yx}\,[\boldsymbol{x}(t)]^{+} \end{aligned} \tag{1}$$

where $\boldsymbol{x}$, $\boldsymbol{y}$, $\boldsymbol{z}$ are the neural activations of MC, MC-layer4 (MC-L4) and thalamus, respectively. $[]^{+}$ is the ReLU Activation Function. $\boldsymbol{K}_{xz}$ is the MC-L4 to MC connectivity matrix, $\boldsymbol{K}_{zy}$ is the thalamus to MC-L4 connectivity matrix, $\boldsymbol{K}_{yx}$ is the MC to thalamus connectivity matrix. Note, $\boldsymbol{K} = \boldsymbol{K}_{xz}\boldsymbol{K}_{zy}\boldsymbol{K}_{yx}$ summarizes these three connectivity matrices around the loop into one feedback gain matrix, which can be calculated from the method described in (Kao et al., 2021).

For the dynamics of MC, $\tau = 200$ is the time constant of MC dynamics. $\boldsymbol{W}$ is the recurrent weight matrix specified in next subsection. $\boldsymbol{\zeta}(t) = \boldsymbol{z}_{sp} + \boldsymbol{z}_{ci} + \boldsymbol{z}_{pp}$ denotes all the inputs. $\boldsymbol{z}_{sp(t)} = \boldsymbol{x}_{sp} - \boldsymbol{W}[\boldsymbol{x}_{sp}]^{+}$ maintains the spontaneous activity of the network. $\boldsymbol{z}_{ci}$ is the condition-independent signal, appears after the go cue and induces a substantial change in dynamics (Kaufman et al., 2016; Kao et al., 2021):

$$\boldsymbol{z}_{ci}(t) = \boldsymbol{a} \times \begin{cases} exp\left(\frac{t_{\text{go}}-t}{600}\right) - exp\left(\frac{t_{\text{go}}-t}{60}\right) & t > t_{\text{go}} \\ 0 & t \le t_{\text{go}} \end{cases} \tag{2}$$

where $\boldsymbol{a} = 7.28 + \boldsymbol{\zeta}$. $\boldsymbol{\zeta}$ is a N dimensional vector sampled from Gaussian distribution $\mathcal{N}(0, 0.2)$. t_{go} is the time when go cue onset. As the $\boldsymbol{x}(\boldsymbol{t}_{\text{go}})^{*} > 0$ in setup, the network could be approximated as a linear dynamical system. Thus, the input $\boldsymbol{u}^{t}$ denoting the target position is defined as:

$$\boldsymbol{u}^{t} = \alpha \times (\boldsymbol{\Delta x}^{t} - \boldsymbol{W}\boldsymbol{\Delta x}^{t}) \tag{3}$$

where $\alpha = 2.7$ is hyper-parameters. The control input defined as:

$$\boldsymbol{u}^{*} = \boldsymbol{x}^{*} - (\boldsymbol{W} + \boldsymbol{K})[\boldsymbol{x}^{*}]^{+} - \boldsymbol{\zeta} - \boldsymbol{u}^{t} \tag{4}$$

was switched off at go cue onset. $\boldsymbol{z}_{pp}$ is the proprioceptive input (further specified below).

Finally, MC are readout into muscle activity through a output layer, defined as:

$$\tau_{m}\frac{d\boldsymbol{m}}{dt} = -\boldsymbol{m}(t) + [\boldsymbol{C}\boldsymbol{r}(t)]^{-} \tag{5}$$

where the readout weight matrix $\boldsymbol{C}$ is sampled from Gaussian distribution $\mathcal{N}(0, 0.1^{2}/N)$, and $\tau_{m} = 50$ ms is the time constant. $[]^{-}$ is the LeakyReLU Activation Function with negative slope equal to 0.4.

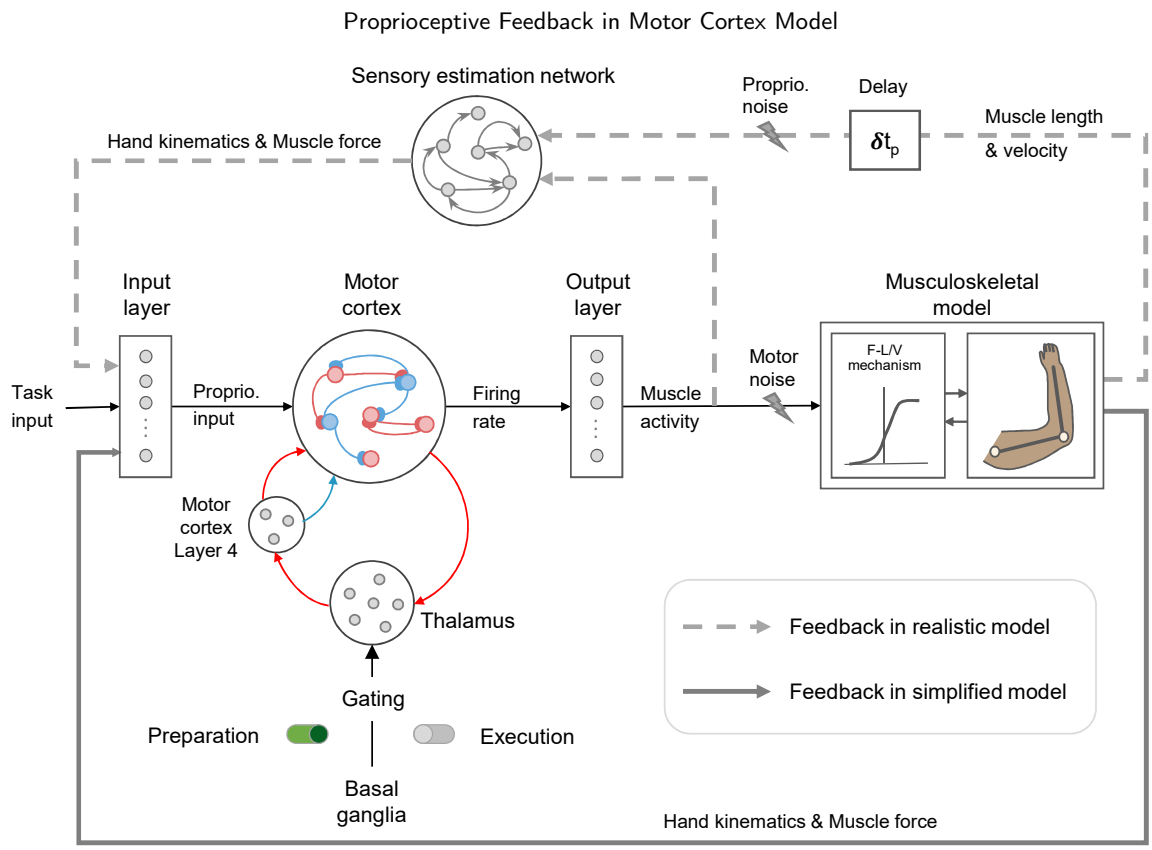

Figure 2: Schematics of the model framework. The core of this framework is the thalamocortical loop which only works in the preparation epoch to evolve the MC network to the proper initial conditions. The firing rates generated by MC network are translated into muscle activity via the output layer. Then, the noisy muscle activity is converted into muscle force through F-L/V mechanism, actuating the motion of the two-link arm model. MC receives task and proprioceptive inputs during movement execution. There are two types of models based on different proprioceptive feedback structures. First, the simiplified model is in an ideal situation where proprioceptive input is from hand kinematics and force directly without any noise and delay (dark grey line). Second, the complete model receives the output of the sensory estimation network, which estimate the proprioception from delayed and noisy muscle length and velocity, as well as muscle activity (grey dashed line).

2.1.2. Motor cortex network

We modeled the MC as an biologically plausible network, inhibition-stabilized network (ISN), satisfying Dale's law (neurons are either excitatory or inhibitory) (Hennequin et al., 2014; Eskikand et al., 2023). ISN can produce rich and naturalistic neural responses. Our ISN comprised 300 excitatory and 100 inhibitory neurons ($N = 400$), with a similar neuron proportion to that in the MC of non-human primates (Bakken et al., 2021; Chen et al., 2023).

Initially, we constructed a random connectivity matrix of size $N \times N$ with a connectivity density $p = 0.1$. The non-zero excitatory weights were drawn from a lognormal distribution with mean $log(w_0)$ and variance 1, where $w_0^2 = r^2/(p(1-p))$, $r = 1.2$. For inhibitory weights, we employed a uniform distribution between -1 and 0. The random excitatory weights are stabilized by fine-tuned inhibitory architecture (Hennequin et al., 2014). We optimized the inhibitory synapses to minimize the "smoothed spectral abscissa" α_ϵ, the greatest real part of $\boldsymbol{W}$'s eigenspectrum, to below 0.9. The gradient of smoothed spectral abscissa with respect to the connectivity matrix is expressed as:

$$\frac{d\alpha_\epsilon(\boldsymbol{W})}{d\boldsymbol{W}} = \frac{\boldsymbol{OP}}{tr(\boldsymbol{OP})} \tag{6}$$

where $\boldsymbol{O}$ and $\boldsymbol{P}$ are respectively the observability and controllability Gramians of the system, defined as:

$$\begin{aligned} \boldsymbol{O} &= \frac{2}{\tau}\int_0^\infty e^{(\boldsymbol{W}^T-\boldsymbol{I})t/\tau} e^{(\boldsymbol{W}-\boldsymbol{I})t/\tau} dt \\ \boldsymbol{P} &= 2\int_0^\infty e^{t(\boldsymbol{W}-\boldsymbol{I})} e^{t(\boldsymbol{W}-\boldsymbol{I})^T} dt \end{aligned} \tag{7}$$

where $\boldsymbol{I}$ is the unit matrix.

In 3.4, the 'dynamic-direction' that evokes the most energy variation (Hennequin et al., 2012a) of the network dynamics is the first eigenvector of the observability Gramians, $\boldsymbol{O}$. The 'output-direction' that evokes the most energy variation of the readout (Kao et al., 2021) is the first eigenvector of the modified observability Gramians:

$$\boldsymbol{O}_{out} = \frac{2}{\tau}\int_0^\infty e^{(\boldsymbol{W}^T-\boldsymbol{I})t/\tau} \boldsymbol{C}^T\boldsymbol{C} e^{(\boldsymbol{W}-\boldsymbol{I})t/\tau} dt \tag{8}$$

Observability and controllability Gramians can be solved from Lyapunov equation.

2.1.3. Musculoskeletal Arm model

The two-link musculoskeletal arm model is in the horizontal two-dimensional plane, driven by six lumped muscles (mono-articular shoulder flexors, mono-articular shoulder extensors, mono articular elbow flexors, mono-articular elbow extensors, biarticular flexors and biarticular extensors) (Lillicrap and Scott, 2013). First, muscle activity $\boldsymbol{m}(t)$ was transformed into muscle force $\boldsymbol{f}(t)$ via the force-length-velocity function:

$$\boldsymbol{f}(t) = F_{lv}\boldsymbol{m}(t) \tag{9}$$

where $F_{lv} = F_l(\boldsymbol{l}) \cdot F_v(\boldsymbol{l}, \dot{\boldsymbol{l}})$ is the force-length-velocity function (the parameters are in appendix):

$$\begin{aligned} F_l(\boldsymbol{l}) &= \exp\left(-\text{abs}\left(\frac{\boldsymbol{l}^{\beta}-1}{\omega}\right)^{\rho}\right) \\ \mathrm{F}_v(\boldsymbol{l}, \dot{\boldsymbol{l}}) &= \begin{cases} \frac{V_{\max}-\dot{\boldsymbol{l}}}{V_{\max}+(c_{V0}+c_{V1})\dot{\boldsymbol{l}}} & \dot{\boldsymbol{l}} \leq 0 \\ \frac{b_V-\left(a_{V0}+a_{V1}l+a_{V2}l^2\right)\dot{l}}{b_V+\dot{l}} & \dot{\boldsymbol{l}} \leq> 0 \end{cases} \end{aligned} \tag{10}$$

where $\boldsymbol{l} = (l_1, l_2, \ldots, l_6)$ and $\dot{\boldsymbol{l}} = (\dot{l}_1, \dot{l}_2, \ldots, \dot{l}_6)$ are the length and velocity of each muscle, defined as:

$$\begin{aligned} l_i &= 1 + \frac{A_{1i}\left(\theta_{1i}^0 - \theta_1\right)}{L_i^0} + \frac{A_{2i}\left(\theta_{2i}^0 - \theta_2\right)}{L_i^0} \\ \dot{l}_i &= -\frac{A_{1i}\dot{\theta}_1}{L_i^0} - \frac{A_{2i}\dot{\theta}_2}{L_i^0} \end{aligned} \tag{11}$$

where $(\boldsymbol{\theta}, \dot{\boldsymbol{\theta}}) = ((\theta_1, \theta_2)^T, (\dot{\theta}_1, \dot{\theta}_2)^T)$ includes the angles and velocities of the elbow and shoulder joints, which are initialized with the parameters in Table 1 at the trial beginning. A is the moment arm matrix, $\boldsymbol{L^0}$ is the optimal length matrix and $\boldsymbol{\theta^0}$ are the and joint angle. These parameters are defined in the appendix.

The muscle force was mapped into joint torques with a delay of $\delta_f = 100$ ms, as the time when muscle activity begin to change lead movement onset in the experimental observations (Sussillo et al., 2015):

$$\boldsymbol{j}(t) = \boldsymbol{A}\boldsymbol{f}(t - \delta_f) \tag{12}$$

The joint kinematics evolved dynamically according to:

$$\ddot{\boldsymbol{\theta}} = \mathcal{M}(\boldsymbol{\theta})^{-1}\left(\boldsymbol{j}(t) - \mathcal{X}\left(\boldsymbol{\theta}, \dot{\boldsymbol{\theta}}\right) - \mathcal{B}\dot{\boldsymbol{\theta}}\right) \tag{13}$$

where $\mathcal{M}$ is the inertia matrix, $\mathcal{X}$ is the centripetal and Coriolis forces, and $\mathcal{B}$ is the damping matrix representing joint friction. The above parameters are given by

$$\begin{aligned} \mathcal{M}(\boldsymbol{\theta}) &= \begin{pmatrix} a_1 + 2a_2 cos\theta_2 & a_3 + a_2 cos\theta_2 \\ a_3 + a_2 cos\theta_2 & a_3 \end{pmatrix} \\ \mathcal{X}\left(\boldsymbol{\theta}, \dot{\boldsymbol{\theta}}\right) &= a_2 sin\theta_2 \begin{pmatrix} -\dot{\theta}_2\left(2\dot{\theta}_1 + \dot{\theta}_2\right) \\ \dot{\theta}_1^2 \end{pmatrix} \\ \mathcal{B} &= \begin{pmatrix} 0.05 & 0.025 \\ 0.025 & 0.05 \end{pmatrix} \end{aligned} \tag{14}$$

where $a_1 = I_1 + I_2 + M_2 L_1^2$, $a_2 = M_2 L_1 D_2$, and $a_3 = I_2$. These parameters are given in the Table 1. The hand position, $\boldsymbol{p}$ and velocity, $\dot{\boldsymbol{p}}$ are given by:

$$\begin{pmatrix} p_x \\ p_y \\ \dot{p}_x \\ \dot{p}_y \end{pmatrix} = \begin{pmatrix} \mathrm{L}_1 \cos\theta_1 + \mathrm{L}_2 \cos\theta_a \\ \mathrm{L}_2 \sin\theta_1 + \mathrm{L}_2 \sin\theta_a \\ -\dot{\theta}_1\, \mathrm{L}_1 \sin\theta_1 - \dot{\theta}_a\, \mathrm{L}_2 \sin\theta_a \\ \dot{\theta}_1\, \mathrm{L}_1 \cos\theta_1 + \dot{\theta}_a\, \mathrm{L}_2 \cos\theta_a \end{pmatrix} \tag{15}$$

where $\boldsymbol{p} = (p_x, p_y)^T$, $\dot{\boldsymbol{p}} = (\dot{p}_x, \dot{p}_y)^T$, and $\theta_a = \theta_1 + \theta_2$.

2.1.4. Proprioceptive input and proprioceptive system model

The MC network received a ten-dimensional estimated proprioceptive input $\boldsymbol{I_p}$ including hand position $\boldsymbol{p_{est}}$, and velocity $\dot{\boldsymbol{p}}_{\boldsymbol{est}}$, and muscle force $\boldsymbol{f_{est}}$:

$$\boldsymbol{I_p} = (\boldsymbol{p_{est}}^T, \dot{\boldsymbol{p}}_{\boldsymbol{est}}^T, \boldsymbol{f_{est}}^T/\alpha)^T \tag{16}$$

Thus, the proprioceptive input is denoted as:

$$\begin{aligned} \boldsymbol{I_{pp}} &= \alpha \times (\boldsymbol{B}\boldsymbol{I_p} + \boldsymbol{b_b}) \\ \boldsymbol{z_{pp}} &= \boldsymbol{W}\boldsymbol{I_{pp}} - \boldsymbol{I_{pp}} \end{aligned} \tag{17}$$

where $\boldsymbol{B}$ is an $N \times 10$ weight matrix sampled from Gaussian distribution $\mathcal{N}(0, 1/10)$. Note, the first two columns of $\boldsymbol{B}$ are the $\boldsymbol{b^t}_1$ and $\boldsymbol{b^t}_2$ in the 2.1.5. Thus the MC network thus compared the current hand position to the target position (explained in the appendix). $\boldsymbol{b_b}$ is the bias.

In order to estimate the proprioception from the noisy and delayed proprioceptive feedback and the efference copy of the motor command (muscle activity), we constructed a sensory estimation network based on the gated recurrent unit (GRU) with 200 units. GRU is a streamlined version of the LSTM that often achieves comparable performance but faster computation (Chung et al., 2014). The input to GRU is defined as:

$$\begin{aligned} \boldsymbol{p_t} &= ((\boldsymbol{l}_{t-\delta_p} - \boldsymbol{l^0} + \boldsymbol{\xi_p})^T, (\dot{\boldsymbol{l}}_{t-\delta_p} + \boldsymbol{\xi_p})^T) \\ \boldsymbol{x_t} &= (\boldsymbol{p_t}^T, \boldsymbol{m_t}^T)^T \end{aligned} \tag{18}$$

where l is the muscle length $\dot{l}$ is muscle velocity, and l^0 is the muscle length at the trial beginning. $\delta_p = 35$ ms, as the proprioceptive feedback takes at least 35 ms to reflect on the motor cortical population activity (Pruszynski et al., 2014). ξ_p is the sensory noise (specified in 3.5).

The GRU (Figure A6) consists of two gates. The reset gate controls how much of the previous state to remember, while the update gate determines how much of the new state is a copy of the previous state. For the the hidden state of the previous time step, $\boldsymbol{h_{t-1}}$, the reset gate $\boldsymbol{r_t}$ and update gate $\boldsymbol{u_t}$ are computed as follows:

$$\begin{aligned} \boldsymbol{r_t} &= \sigma(\boldsymbol{W_{rx}}\boldsymbol{x_t} + \boldsymbol{W_{rh}}\boldsymbol{h_{t-1}} + \boldsymbol{b_r}) \\ \boldsymbol{u_t} &= \sigma(\boldsymbol{W_{ux}}\boldsymbol{x_t} + \boldsymbol{W_{uh}}\boldsymbol{h_{t-1}} + \boldsymbol{b_u}) \end{aligned} \tag{19}$$

where $\boldsymbol{W_{rx}}$, $\boldsymbol{W_{ux}}$, $\boldsymbol{W_{rh}}$ and $\boldsymbol{W_{uh}}$ are weight parameters.$\boldsymbol{b_r}$ and $\boldsymbol{b_u}$ are bias. σ is the Sigmoid function.

Then, the candidate hidden state $\tilde{\boldsymbol{h}}_t$ at time t are computed as:

$$\tilde{\boldsymbol{h}}_t = \tanh\left(\boldsymbol{W}_{\boldsymbol{hx}}\boldsymbol{x}_t + \boldsymbol{W}_{\boldsymbol{hh}}\left(\boldsymbol{r}_t \odot \boldsymbol{h}_{t-1}\right) + \boldsymbol{b}_{\boldsymbol{h}}\right) \quad (20)$$

where $\boldsymbol{W}_{\boldsymbol{hx}}$ and $\boldsymbol{W}_{\boldsymbol{hh}}$ are weight parameters. $\boldsymbol{b}_{\boldsymbol{h}}$ is bias. $\boldsymbol{h}$ is bias. $\odot$ the Hadamard (elementwise) product operator. The final GRU update equation is defined as:

$$\boldsymbol{h}_t = \boldsymbol{Z}_t \odot \boldsymbol{h}_{t-1} + \left(1 - \boldsymbol{u}_t\right) \odot \tilde{\boldsymbol{h}}_t \quad (21)$$

The hidden state is mapped into estimated hand kinems and muscle force :

$$\boldsymbol{o}_t = \boldsymbol{W}_{\boldsymbol{oh}}\boldsymbol{h}_t + \boldsymbol{b}_{\boldsymbol{o}} \quad (22)$$

where $\boldsymbol{W}_{\boldsymbol{oh}}$ is weight parameters, and $\boldsymbol{b}_{\boldsymbol{h}}$ is bias. All the parameters in the GRU were sampled from the $\mathcal{N}(0, 0.01)$

2.1.5. Initial condition setup

Neural responses in MC shows an rich transients after go cue onset (Churchland et al., 2012; Shenoy et al., 2013). The neural state at go cue, which is the initial condition in our RNN model and denoted as $\boldsymbol{x}^* = \left(\boldsymbol{x}_1^*, \boldsymbol{x}_2^*, \ldots, \boldsymbol{x}_8^*\right)$, is defined as:

$$\boldsymbol{x}_k^* = \boldsymbol{x}_{\boldsymbol{sp}} + \sum_{i=1}^{2} \boldsymbol{b}^{\boldsymbol{t}}{}_i p_{k,i}^* + \sum_{i=1}^{N} Z_{k,i}\boldsymbol{a}_{\boldsymbol{i}} = \boldsymbol{x}_{\boldsymbol{sp}} + \boldsymbol{\Delta x}^{\boldsymbol{t}} + \boldsymbol{\Delta x}^* \quad (23)$$

where $\boldsymbol{x}_{\boldsymbol{sp}}$ is the spontaneous activity sampled from Gaussian distribution $\mathcal{N}(20, 9)$ throughout all task phases. $\boldsymbol{p}_{\boldsymbol{k}}{}^*$ is the target position with the angle of θ_k^{targ} and the distance of 15 cm from the origin (see in Table 1), $\boldsymbol{b}^{\boldsymbol{t}}{}_i$ is an N dimensional weight vector sampled from Gaussian distribution $\mathcal{N}(0, 1/I)$. $I = 10$ is the number of the external input. $\boldsymbol{a} = \left(\boldsymbol{a}_{\boldsymbol{1}}, \boldsymbol{a}_{\boldsymbol{2}}, \ldots, \boldsymbol{a}_{\boldsymbol{N}}\right)^T$ is the full eigenvectors of $\boldsymbol{O}$, ordered by decreasing eigenvalues, and $\boldsymbol{Z}$ is a weight matrix sampled from Gaussian distribution $\mathcal{N}(0, 1.5/N)$. The initial conditions contains the information about spontaneous background activity, target position and various transient behaviors.

Following Kao et al. (2021), we scale the variance of firing rates after go cue to $\sigma_{reach}^2 = 16$ Hz.

2.2. Model optimization

For computational convenience, we first built a simplified model assuming proprioception without delay and noise (Figure 2, grey line). We starts the simulation from go cue onset (t_{go}) and utilized the Euler integration with time steps of $dt = 10$ ms. The proprioceptive input is:

$$\boldsymbol{I}_{\boldsymbol{p}}(t) = (\boldsymbol{p}(t-1)^T, \dot{\boldsymbol{p}}(t-1)^T, \boldsymbol{f}(t-1)^T/\alpha)^T \quad (24)$$

After training the simplified model, we set $dt = 1$ ms and get the optimized parameters. Considering the real proprioceptive pathway, we trained sensory estimation network and incorporated it into the realistic model (Figure 2, grey dashed line). We started the simulation at the trial beginning (MC at spontaneous activity), by Euler integration with time steps of $dt = 1$ ms.

2.2.1. Training simplified model

In the reach task, the network was required to control the arm model to reach the target within 1000 ms after go cue. We first trained a simplified model in the absence of sensory and motor noise, using the Adam optimizer with a learning rate of 2×10^{-4} and 1000 iterations. Before optimization, the initial conditions x_k^* and spontaneous activity x_{sp} were restricted in the nullspace of $\boldsymbol{C}$ to prevent movement from occurring at the end of preparation and spontaneously. The loss function are composed of the MSE between the network output and the target at the end of the movement, and a penalization term:

$$\mathrm{L} = \frac{10}{8}\left(\mathrm{L}_0 + \mathrm{L}_1 + \mathrm{L}_2\right) \quad (25)$$

First, the network should hold the arm model for a $\mathrm{T}_0 = 300$ ms after reaching the target, where hand velocity is nearly zero.

$$\mathrm{L}_0 = \frac{1}{T_0}\sum_{k=1}^{8}\int_{\mathrm{t_{end}}-T_0}^{\mathrm{t_{end}}} \left\|\boldsymbol{p}_k(t) - \boldsymbol{p}_k^*\right\|^2 + \left\|\dot{\boldsymbol{p}}_k(t)\right\|^2 dt \quad (26)$$

where k is the number of movement condition and $\mathrm{t_{end}} = 1200$ ms. Moreover, we also penalized muscle activity to prevent undue muscle output at the end of the movement:

$$\mathrm{L}_1 = \frac{1}{T_1}\sum_{k=1}^{8}\int_{\mathrm{t_{end}}-T_1}^{\mathrm{t_{end}}} \left\|\boldsymbol{m}_k(t)\right\|^2 dt \quad (27)$$

where $\mathrm{T}_1 = 200$ ms.

Second, we reduce the model and monkey data to ten dimensions by PCA and sample the reduced model data every three time points to have the same time length with monkey data. We regularized the neural dynamics in a low-dimensional space:

$$\mathrm{L}_2 = \alpha \mathrm{R}_o + \beta \mathrm{R}_n \quad (28)$$

where $\alpha = 9 \times 10^{-3}$, $\beta = 10^{-4}$ are the penalization weights.

The first term penalizes oscillation in the first two principle components (PCs), as we observed that the first two PCs of real data are generally α-shaped:

$$\mathrm{R}_o = \frac{1}{T_h}\sum_{k=1}^{8}\sum_{i=1}^{2}\int_{\mathrm{t_{go}}}^{\mathrm{t_{go}}+T_h} \left\|\boldsymbol{s}_{k,i}(t) - \boldsymbol{s}_{k,i}(t_{go} + T_h - t)\right\|^2 dt \quad (29)$$

where $\boldsymbol{s} \in \boldsymbol{R}^{8\times10\times t}$ is the PCs, where $t = 840$ is the number of time points, $c = 8$ $T_h = 420$ ms.

The second term penalizes the temporal distribution of the sixth to the tenth principle components (PCs). If there was no penalization, these PCs would quickly decay to zero. Thus, we required that the value of these PCs at the first half of movement was no stronger than that of the latter half:

$$\mathrm{R}_n = \frac{1}{T_h} \max\left(0, \sum_{k=1}^{8}\left(\int_{\mathrm{t_{go}}}^{\mathrm{t_{go}}+T_h} \left\|\boldsymbol{s}_{k,i=6,\ldots,10}(t)\right\|^2 dt - \int_{\mathrm{t_{go}}+T_h}^{\mathrm{t_{go}}+2T_h} \left\|\boldsymbol{s}_{k,i=6,\ldots,10}(t)\right\|^2 dt\right)\right) \tag{30}$$

The recurrent architecture of the MC remains fixed after 2.1.2. We optimized movement-specific initial condition $\boldsymbol{x}^*$, input weight matrix $\boldsymbol{B}$ and readout matrix $\boldsymbol{C}$ in the standard MC network.

2.2.2. Training sensory estimation network

After the optimization of the baseline model, we replaced the direct feedback by the sensory estimation network, which estimate the current hand kinematics and muslce force from muscle kinematics and efference copy of the motor command. We used the Adam optimizer with a learning rate of $5 \times 10^{-}4$ and 1000 iterations and exclude sensory noise during training (ξ_p). The loss function was the vector norm between the estimated and the actual proprioception:

$$\mathrm{L} = \frac{1}{8T}\sum_{k=1}^{8}\int_{\mathbf{t}_{\mathrm{go}}}^{\mathbf{t}_{\mathrm{end}}} \left\|o_k(t) - o_k(t)^*\right\|^2 dt \tag{31}$$

where $\boldsymbol{o_k(t)}^*$ is composed of the actual hand velocities and muscle force. The set of parameters to be optimized is $(\boldsymbol{W_{rx}}, \boldsymbol{W_{ux}}, \boldsymbol{W_{rh}}, \boldsymbol{W_{uh}}, \boldsymbol{W_{hx}}, \boldsymbol{W_{hh}}, \boldsymbol{W_{oh}}, \boldsymbol{b_r}, \boldsymbol{b_u}, \boldsymbol{b_h}, \boldsymbol{b_o})$. Sensory noise was not present during training.

2.2.3. Training realistic model

In the real world, arm operates in a relatively unpredictable environment with sensory and motor noise. Therefore, motor noise was added to the motor commands (muscle activity), while sensory noise was added to the proprioceptive feedback:

$$\begin{aligned} \boldsymbol{m}(t) &= \boldsymbol{m}(t) + \boldsymbol{\xi_m}\boldsymbol{m}(t) \\ \boldsymbol{p}(t) &= \boldsymbol{p}(t)s + \boldsymbol{\xi_p} \end{aligned} \tag{32}$$

where $\boldsymbol{\xi_m}$ and $\boldsymbol{\xi_p}$ were randomly sampled from Gaussian distribution $\mathcal{N}(0, 0.05)$. The loss function is defined as:

$$\mathrm{L} = \frac{1}{8T}\sum_{k=1}^{8}\int_{\mathbf{t}_{\mathrm{end}}-T}^{\mathbf{t}_{\mathrm{end}}} \left\|\boldsymbol{p}_k(t) - \boldsymbol{p}_k^*\right\|^2 + \|\dot{\boldsymbol{p}}(t)\|^2 dt \tag{33}$$

where $T = 1200$ ms and $t_{end} = 300$ ms.

Only the initial conditions $\boldsymbol{\Delta x}^*$ was optimized and restricted in the nullspace of the readout matrix $\boldsymbol{C}$ and scaled the variance of firing rates during training. We used the Adam optimizer with a learning rate of $3 \times 10^{-}3$ and 50 iterations.

2.3. Statistical analysis

2.3.1. Preprocessing and Principal component analysis

Neural recording were made from the primary motor cortex (M1) and dorsal premotor cortex (PMd) of Macaque monkey C and M using Utah electrode arrays (Gallego et al., 2020; Gallego-Carracedo et al., 2022; Safaie et al., 2023). Here, We analysed one session of the recordings (268 neurons for monkey C, and 98 neurons for monkey M) and obtained the firing rates following the same procedure described in Safaie et al. (2023). We applied a Gaussian kernel ($\sigma = 50$ ms) to the binned square-root transformed spike counts (bin size 30 ms) of each neuron, and excluded neurons whose mean firing rate less than 1 Hz. Firing rates were computed separately for the movement preparation and execution periods: a 1000 ms window starting 200 ms before target onset, and a 1000 ms window starting 300 ms before movement onset.

The movement onset in our model is defined as time when hand velocity begins to change, however, this subtle change is difficult to detect in the experiment. In the analysis of execution period, We set a 1000 ms window starting 250 (150) ms before movement onset (go cue), leaving 50 ms for the detectable changes of hand velocity. Considering the external stimuli takes at time to influence cortical responses and trial variability, we select a period starting t_r (drawn i.i.d. from $\mathcal{N}(150, 20)$) before go cue. We perform such temporal alignment when comparing model and real data.

We produced a data matrix $\boldsymbol{X} \in \boldsymbol{R}^{\mathrm{n}\times ct}$, where n is the number of neurons, c is the number of reach conditions, and t is the number of time points. Then we 'soft' normalized each neuron's firing rate (fr): $fr = fr/(range(fr)+5)$, and mean-centered fr so that each neuron has a zero mean (Churchland et al., 2012). We used Principal component analysis (PCA) to reduce the dimensionality of data $\boldsymbol{X_{red}} \in \boldsymbol{R}^{\mathrm{n}\times ct}$, where k is the number of principal components (PCs).

2.3.2. Demixed principal component analysis

Demixed principal component analysis (dPCA) (Brendel et al., 2011; Kobak et al., 2016) utilizing information discarded by PCA, demixing the components tuning to the task parameters. dPCA seeks to find a transformation matrix $\boldsymbol{W}$, which projects the data matrix $\boldsymbol{R}$, onto a lower-dimensional space $\boldsymbol{X}$ through the equation that $\boldsymbol{X} = \boldsymbol{RW}$, where each row of $\boldsymbol{R}$ indicates the condition and time points of firing rates, each column of $\boldsymbol{W}$ represents a new dimension, and each column of $\boldsymbol{X}$ represents a component of the population response. Importantly, the key difference between dPCA and PCA is that dPCA seeks a transformation that not only captures variance but also aligns the principal components with the conditions or time indicated by the labels. Therefore, dPCA found some components (columns of $\boldsymbol{X}$) varying over time while being constant across conditions, and others varying across conditions while staying constant over time. We divided these two components into: condition-independent and condition-dependent.

In this paper, we performed dPCA on monkey data in a 1020 ms period starting 300 ms before movement onset and extracted the first fifteen components. As the time points of monkeys' firing rates are too few to be applied PCA, we interpolated the monkey data every three time points

by cubic interpolation; we ignored noise covariance within trials.

2.3.3. Orthogonal Canonical Correlation Analysis

The Orthogonal canonical-correlation analysis (CCA) method (Cunningham and Ghahramani, 2015; Russo et al., 2018) is an extension of the traditional CCA that enforces an orthogonality constraint on the transformations, leading to uncorrelated components within each dataset. The similarity between mean-centered datasets $\boldsymbol{X_a} \in \boldsymbol{R}^{k\times ct}$ and $\boldsymbol{X_b} \in \boldsymbol{R}^{k\times ct}$ is:

$$\underset{M_a,M_b}{\operatorname{argmax}} \frac{\operatorname{tr}\left(M_a^\top X_a X_b^\top M_b\right)}{\sqrt{\operatorname{tr}\left(M_a^\top X_a X_a^\top M_a\right)\operatorname{tr}\left(M_b^\top X_b X_b^\top M_b\right)}} \quad (34)$$

where M_a and M_b are orthonormal matrices. Similarity will be unity if two datasets are the same. We focused on a 1020 ms period starting 300 ms before movement onset. We first sample the model data every three time points, making the two datasets have the same time length. Then we reduce the dimensions by PCA (k=10), which ensures that correlations were not driven by low-variance data (Sussillo et al., 2015). Finally, we compute the similarity.

2.3.4. Procrustes analysis

Procrustes analysis is a statistical method used to compare two sets of shape data by minimizing the sum of squared differences between corresponding points in the two sets. The method involves scaling, rotating, and translating one set of data to optimally superimpose it onto the other set. We used Procrustes analysis to compare the PCs of model and real data. To assess the goodness of fit, we calculated the M^2, which is the sum of the squares of the point-wise differences between the two datasets. M^2 is 0 indicates a perfect fit, while 1 indicates a poorer fit.

2.3.5. Population ratio

As illustrated in Figure 5B, C, the population ratio quantifies the changes in population activity after different disruptions, defined as:

$$\|x_{dis}(t) - x_{sp}\| / \|x_{ctr}(t) - x_{sp}\| \quad (35)$$

where $x_{dis}(t)$ is the neuronal activity in disruption trial, $x_{ctr}(t)$ is the neuronal activity in control trial. We first removed the spontaneous activity and computed the magnitude of the population activity, which is the vector norm across all neurons. We then compared this magnitude to that in control trial, and averaged the ratio across all conditions.

3. Results

3.1. Model with proprioceptive feedback resembles the real data

Our optimized MC network model completes the delayed reach task, with similar behavioral performance across trials but trial-to-trial variability within each condition (Figure 3A, A1A). The firing rates of individual neurons separated across movement conditions were similar to those observed in monkey data: some neurons display homogeneous, while others display multiphase and heterogeneous firing pattern after movement onset (Figure 3B).

To examine the main characteristics of the population response, we identified condition-independent (identical across conditions) and condition-dependent (condition specific) components of the population response during the transition from preparing to executing a reaching (in a 1s window starting before movement onset) via dPCA (Brendel et al., 2011; Kobak et al., 2016). dPCA explains nearly the same amount of variance as PCA on both monkey and model data (top of Figure 3C, E). Condition-independent components capture 54 % variance of monkey C data, 55 % variance of model data (bottom of Figure 3C, E), indicating that the contribution of variance explained by components from real data and model are highly consistent. These results are comparable to the previous finding that the largest component in motor cortical activity is condition-independent (Kaufman et al., 2016). The two labeled components of model and real data also rank in a similar order. Additionally, the temporal evolution of individual demixed principal components of monkey and model are qualitatively similar (Figure 3D, F). For the condition-independent components, the first component displays rapid rise before movement onset and slow decay after that, while the second exhibits a bump before movement onset and then decay. The third component of monkey and model are almost identical. For the condition-dependent components, the absolute values of the first two components increase after movement onset and then decrease, while the sign of the third component inverses during movement execution. Additionally, the model's overall trends of components also closely mirror the trends in the monkey M data. However, the largest component in the monkey M data is condition-dependent (Figure A1B, C), as most of the recorded neurons are heterogeneous.

Moreover, the MC network also display temporal patterns comparable to those observed in previous studies during reaching. First, we find a ring-like structure after applying PCA to firing rates around the go cue (Figure A1B), as reported by Even-Chen et al. (2019). Second, the MC network displays rotational dynamics (Figure (Churchland et al., 2012)A), similar to those in the real data (Figure A2). However, the fitting quality is low in monkey data (Figure A2B). This discrepancy might be due to differences in the analysis window and the identification of movement onset.

To assess the similarity model and real neural response, we first applied a modified CCA (Cunningham and Ghahramani, 2015), which finds linear transformations of two datasets to maximize their correlation. The similarity between model and monkey C (M) is 0.88 (0.85). Moreover, we used Procrustes analysis (PA), which quantifies the degree of alignment between two datasets by M^2 statistic, with a lower M^2 indicating more similar. The M^2 of model and

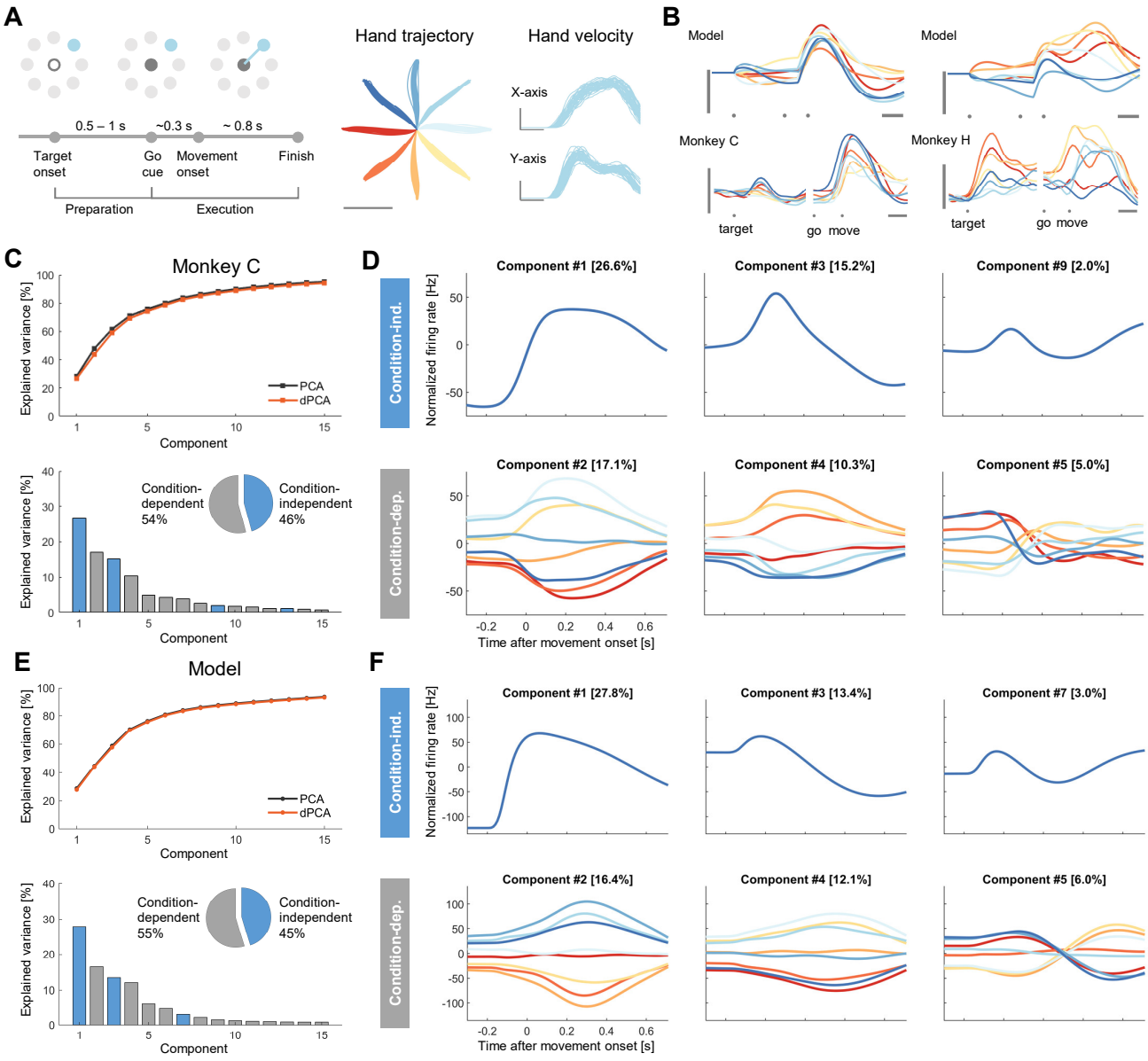

Figure 3: Neural population dynamics of monkey and model during reaching. (A) The simulation of the delayed reach task. Left: the schematic of the task indicating important time point and period for analysis. Middle and right: Behaviour performance of the model. hand trajectories (middle) from 40 trials; horizontal bar: 0.1 m. X and Y hand velocities of the upper-right movement condition after go cue(right); vertical bar: 0.1 m/s, and horizontal bar: 200 ms. (B) Firing rates of representative neurons in the model and monkey. Traces are colored according to the hand trajectories. Vertical bar: 20Hz, and Horizontal bar: 200 ms. (C) Variance captured by dPCA components for monkey C data. Top: cumulative variance explained by dPCA (black) and PCA (orange). Bottom: bars show the variance of the individual demixed principal components. Gray for condition-independent signal, and blue for condition-dependent signal. Pie chart shows the proportions of each signal. (D) Demixed principal components for monkey C data. Top: first three components for condition-independent signal. Bottom: first three components for condition-dependent signal. (E, F) Same as (C, D) except for model data.

monkey C (M) is 0.23 (0.27). These results demonstrate our model is in good agreement with the MC data.

In summary, our MC network model has successfully replicated key features of MC activity in reach task, setting the first stage for further investigations into the cortical pattern generation.

3.2. Necessity of recurrent structure and proprioceptive feedback

So far we have shown the similarity between model and real data, we ask whether the recurrent architecture resembles the dynamics in MC, or proprioceptive feedback

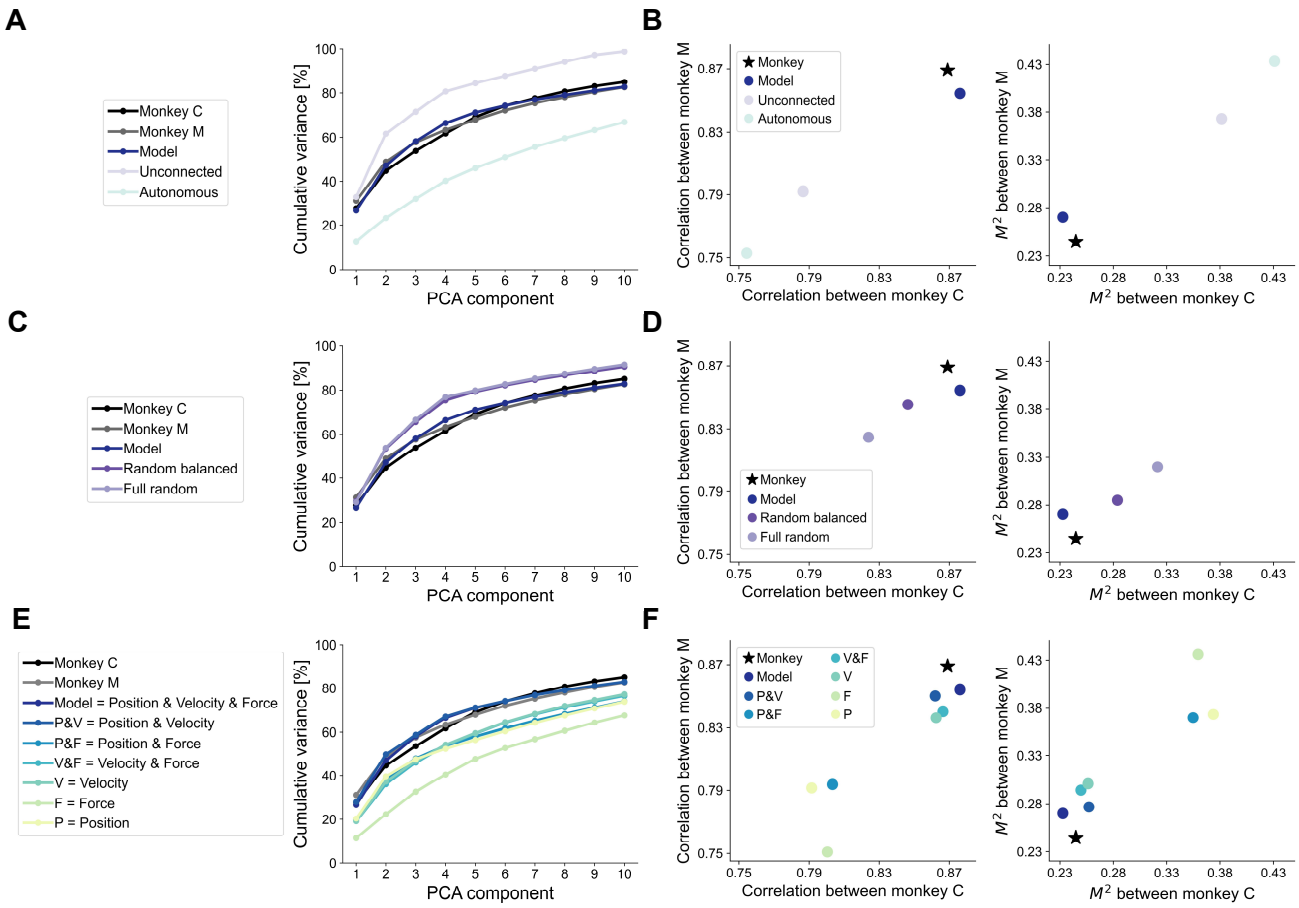

Figure 4: Comparison of the simulated and real population responses. (A) Cumulative variance explained by first ten PCs of monkey C, monkey M, the proposed, unconnected and autonomous model. (B) The similarity between the simulated and real data. Left: the canonical correlation between simulated and monkey M data against the canonical correlation between simulated and monkey C data. Right: the M^2 between simulated and monkey M data against the M^2 between simulated and monkey C data. The similarity between monkey M and monkey C data is shown in black star. (C, D) Same as (A, B) except for random balanced and full random models. (E, F) Same as (A, B) except for models with different combinations of proprioceptive feedback.

is the key factor of motor cortical dynamics? To investigate the contribution of internal dynamics and proprioceptive feedback when modeling, we built a network without recurrent connectivity (unconnected), and an autonomous network which does not receive proprioceptive feedback. After optimization, the first ten PCs of unconnected network explained too much variance, while the first ten PCs of autonomous network explained too little (Figure 4A). For the quantitative analysis, these networks are less similar to the monkey data compared to the proposed model, where the autonomous network is the least similar to real data (Figure 4B). Moreover, for the dPCA results of unconnected network, there is small amount of CIS and the changes in condition-dependent component lag behind that in the real data (Figure A3). For the dPCA results autonomous network, fluctuations in the condition-dependent component are suppressed. In sum, lack of connectivity and proprioceptive feedback reduces the similarity between the model and the real data. Both intrinsic connection and proprioceptive feedback are necessary to produce brain-like signals.

The above results emphasize the necessity of connectivity and proprioceptive feedback in modeling MC. we further constructed several models to confirm that the similarity between model and real data is not a trivial consequence of any type of recurrent connection or proprioceptive feedback. First, we constructed networks with different recurrent connectivity: a random balanced network (Hennequin et al., 2012b) whose connectivity matrix still satisfies Dale law , and a full random network whose connectivity matrix is sampled from the Gaussian distribution $\mathcal{N}(0, 1/N)$ (see eigenvalues of connectivity matrix in FigureA4). The first ten PCs of two networks explain similar variance, but the random balanced network is more similar to real data than full random network, indicating that the MC dynamics would be captured by structured and "less random" networks (Hennequin et al., 2012b). Subsequently, we decoupled the proprioceptive feedback and built a series of models with different combinations of proprioceptive feedback. For the cumulative neural variance, the networks that receive the hand kinematics (positions) plus muscle force and only receive hand kinematics (P&V) have similar results to real

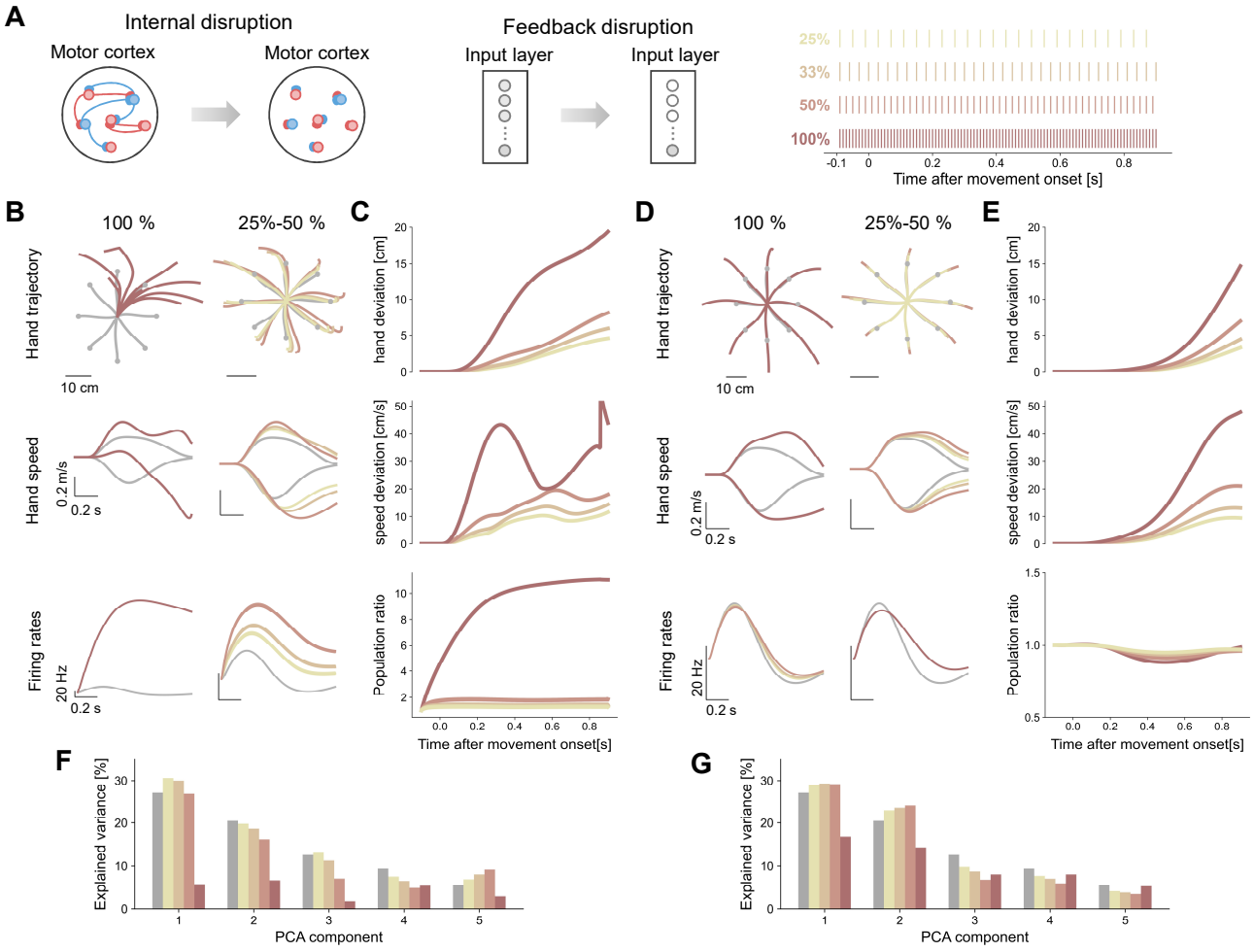

Figure 5: The contribution of internal dynamics and proprioceptive feedback. (A) Illustration of graded disruption. The weights of internal recurrent connections or proprioceptive inputs was set to zero from 25% to 100% timecourse at equal time intervals, respectively. Note, the target input was preserved. (B) The influence of internal dynamics disruption on hand movement and neuronal response. 100% disruption is shown individually, while 25% - 50% are shown together. Top: hand trajectory after disruption compared to the control trial. Middle: x-y hand velocity in condition 1 after disruption compared to the control trial. Bottom: an example neurons' firing rates in condition 1 after disruption compared to the control trial. (C) The changes of hand movement and neuronal response after internal dynamics disruption. Top: condition-averaged Euclidean distance from the hand position to the control hand position at the same time point for different grades of disruption. Middle: condition-averaged Euclidean distance except for hand velocity. Bottom: population ratio that quantifies the firing rate fluctuation relative to that in control trial (D, E) Same as (B, C) except for proprioceptive feedback disruption. (F) Percentage of variance of the control (grey) and internal-disrupted (yellow to pink) activity after projected onto the space spanned by top ten principal components of control activity. (G) Same as (F) except for feedback-disrupted activity.

data, while other models have smaller amounts of variance; the variance of the model only receives muscle force (F) is the smallest. For the quantitative analysis, the proposed model and P&V are most similar to real data; followed by models that receive hand velocity plus force and only receive hand velocity, then models that receive hand position plus force and only receive hand position, and finally model F. Therefore, hand kinematics is important in proprioceptive feedback.

In summary, fine-tuned recurrent structure and proprioceptive feedback are essential in capturing the main aspects of neural population dynamics in MC.

3.3. Internal dynamics dominate in neural population dynamics

From the view of modeling, motor cortical dynamics are generated by internal dynamics and proprioceptive feedback. What are the relative importance of them during movement execution? Does the motor cortical control exhibit a bias towards internal dynamics or proprioceptive feedback? To dissect their contribution, we set internal dynamics (or proprioceptive feedback) to zero while keeping the other component intact. This disruption strategy occurred 25%, 33%, 50%, 100% timecourse at equal time intervals after go cue onset (Figure 5A). Notably, the motor and sensory noise

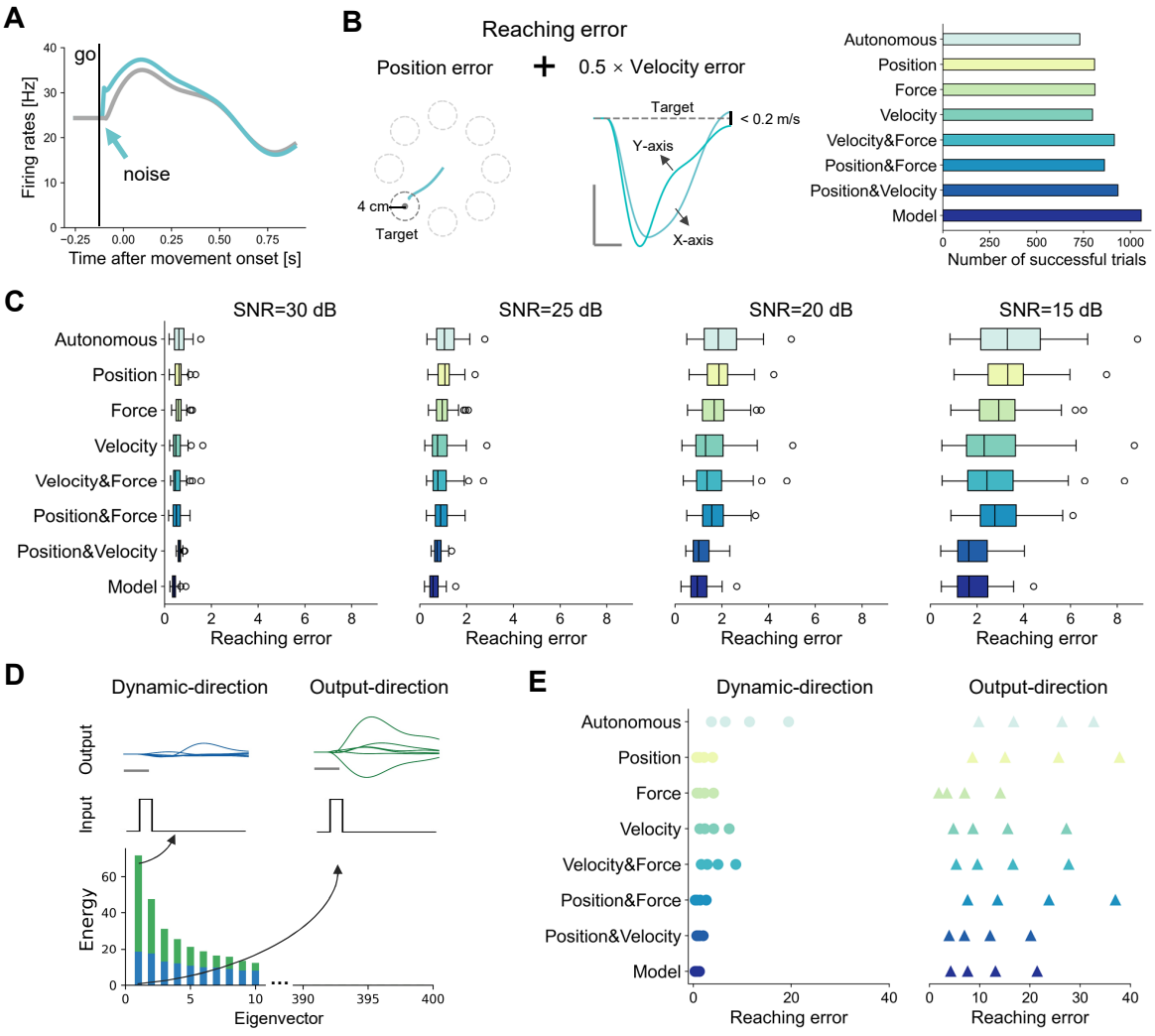

Figure 6: Proprioceptive feedback improves the robustness. (A) Illustration of noise perturbation. Noise is provided to the state of each neuron at go cue onset. Firing rates of an example neuron (cyan) evolve after initial perturbation compared to the control trial (grey). (B) Left: illustration of reaching error which is the sum of position error and 0.5 times velocity error at the end of the movement. Right: number of successful trial of models with different proprioceptive feedback. (C) Box plots of the reaching errors under different SNR conditions of each model. (D) Illustration of the definition of specific noise perturbation, modified from Kao and Hennequin (2019). The eigenvectors of network's observability Gramians define input sensitivity. Input pulses along the 'dynamic-direction' (first blue eigenvector) can trigger large neural responses, while those along the 'output-direction' (first green eigenvector) cause large readouts. (E) Reaching errors under different SNR conditions of each model; circles for dynamic-direction perturbation and triangles for output-direction perturbation.

are set to zero as to prevent other interference beyond the disruption of internal dynamics and proprioceptive feedback. We perform the disruption strategy on the baseline model, a simplified version that does not consider feedback delay and noise. Additionally, we find the 100% internal dynamics disruption drives the arm out of control (Figure A5), which cannot be estimated.

100% internal dynamics disruption has a distinct impact on motor output and neuronal activity compared to other grades. It led to significant deviation from the original hand trajectory and irregular changes on hand velocity, suggesting internal dynamics is critical in guiding the goal of the movement (Top and middle of Figure 5B, C). The network activity 'explodes' without recurrent connection, reflected in a significant increase in the firing rate of single neuron and ten times activation of population responses (Bottom of Figure 5B, C). In addition, the top ten PCs of the activity in the control explain most of the variance, but little variance of the 100% internal-disrupted activity. These results highlight the dominant role of internal dynamics in movement execution. On the other hand, the influence of other internal dynamics disruption increases with the grade regularly. The greater the disruption, the greater the deviation between the actual and the desire movement direction; there is little effect on the explained variance.

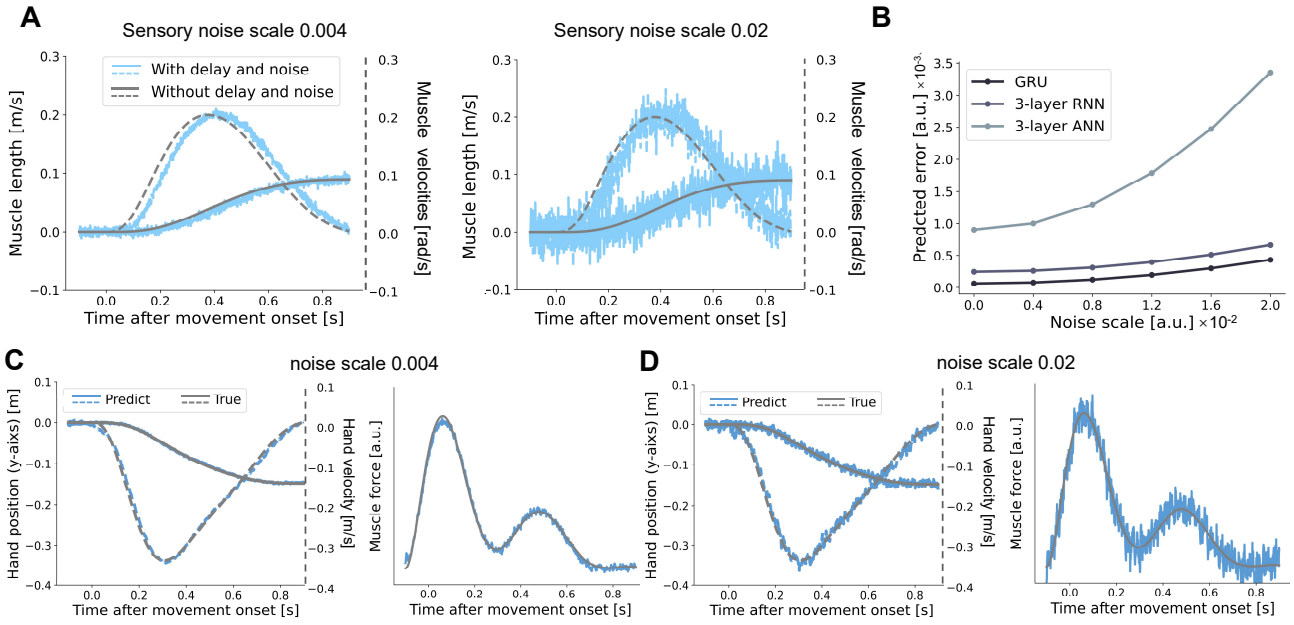

Figure 7: Estimating the arm state from proprioceptive feedback. (A) Proprioceptive feedback under different degree of sensory noise. Proprioceptive feedback includes joint angles (solid traces) and joint velocities (dashed traces). Left: the comparison of actual joint angles and velocities to proprioceptive feedback whose the variance of sensory noise is 0.004. Right: same as the left but the variance of sensory noise is 0.02. Only downward condition was shown for clarity. (B) The squared difference between the real and estimated proprioception under different degree of sensory noise. Black for GRU, dark slate gray for RNN and light slate gray for feedforward network. (C) Predicted proprioception in the case of sensory noise variance of 0.004. Left: the comparison of the predicted to the actual hand positions and velocities. Right: the comparison of the predicted to the actual muscle force. Only downward condition was shown for clarity. (D) Same as the (C) but the variance of sensory noise is 0.02.

In contrast, there are regularities in how different grades of proprioceptive feedback disruption affect motor output. Proprioceptive feedback disruption resulted in ceaseless hand movement towards the target. The greater the disruption grade, the more difficult it is to terminate the movement (Top and middle of Figure 5D, E). Moreover, proprioceptive feedback disruption had little effect on firing rate (Bottom of Figure 5D, E). The influence of the 100% feedback disruption on the explained variance is less than that of the 100% feedback disruption. These results indicate that proprioceptive feedback may be more involved in fine-tuning motor commands rather than generating them.

To summarize, our results show that internal dynamics play a dominant role in generating cortical patterns, whereas proprioceptive feedback is integral to the fine-tuning of motor output.

3.4. Proprioceptive feedback tames sensitivity to initial condition

Initial conditions should tolerate the large neural variability; for example, different initial conditions could result in similar movements (Churchland et al., 2006, 2010). Here, we manipulated the initial conditions into an aberrant state via two strategies: add white Gaussian noise or noise in a specific direction to the initial state (Figure 6A). The strength of the perturbation is quantified by the noise to the initial state with a signal-to-noise ratios (SNRs) of 15, 20, 25 and 30 dB. There are 3200 noisy trials. We define the successful trial as the hand moves within a 4 cm around the target and the norm of velocity at the end of the movement is less than 0.2 within 1 second (Figure 6B, left). In Gaussian noise perturbation, the number of successful trial decrease as the number of the proprioceptive feedback types decreases (Figure 6B, right). Models that receive hand kinematics feedback generate smallest reaching error, followed by models that receive hand velocity plus force and only receive hand velocity, then models that receive hand position plus force and only receive force or hand position, and finally autonomous model (Figure 6C). These results suggest the importance of hand kinematics feedback in against initial noise.

On the other hand, we perturb the initial state in the 'dynamic-direction' that evokes the most energy variation of the network dynamics and the 'output-direction' that evokes the most energy variation of the readout, respectively. These directions are defined by the eigenvectors of the observability Gramians of the network with unit matrix as the readout matrix (dynamic-direction, Figure 6D blue) and the trained readout matrix (output-direction, Figure 6D green), specified in 2.1.2. The results are consistent with that in Gaussian noise perturbation which further confirm the importance of the proprioceptive feedback.

In conclusion, model with proprioceptive feedback executed movement with acceptable deviation under different

types of perturbed initial conditions. Proprioceptive feedback improves the robustness of the network.

3.5. Representation of proprioceptive system

In biologically realistic situations, proprioceptive feedback is always delayed and noisy Crevecoeur et al. (2016). Proprioceptive receptors located in the arm convey muscle information rather than direct hand kinematics Proske and Gandevia (2012). We designed a sensory estimation network that considers delayed feedback and proprioceptive processing. A recent study shows that neurons in proprioceptive system are best tuned to muscle kinematics, and the models optimized to predict the arm state best explains neural representations of proprioception (Vargas et al., 2024). Therefore, our network receive the efference copies of motor command (muscle activity) and muscle length and velocity with different degree of sensory noise (Figure 7A), and then predicts position and velocity of hand and muscle force (Figure 7C, D).

Here, the noise scale s represents standard deviation of the Gaussian distribution $\mathcal{N}(0, s^2)$. This network achieves high predictive accuracy for the arm state (hand position, velocity, and muscle force) even under large sensory noise, demonstrating the model's robustness (Figure 7B). Moreover, we designed other two models with deeper network layers: a three-layer RNN and a three-layer feedforward network. The results of MSE show that the gru-based model is the best at estimating the proprioception even under large noise (Figure 7B, D). In summary, our GRU-based sensory estimation network model accurately and robustly estimates the arm state from noisy and delayed proprioceptive feedback.

4. Discussion

Neural population dynamics have successfully explained the neural basis of movement generation. However, it remains an open question whether the population dynamics in MC are autonomously generated within the neural circuit or driven by external inputs from other brain areas. Theoretical computation found that RNNs with or without external inputs capture many prominent aspects of movement-epoch motor cortical dynamics (Hennequin et al., 2014; Kalidindi et al., 2021; Kao et al., 2021; Pandarinath et al., 2018; Suresh et al., 2020; Sussillo et al., 2015; Zimnik and Churchland, 2021). In this study, we investigated the roles of internal dynamics and proprioceptive feedback in movement execution using an RNN model to perform delayed reach task. Both of the internal dynamics and proprioceptive feedback shape the motor cortical dynamics and physical actions.

First, our model successfully simulate the neuronal activity involved in the delayed-reach task. The single-neuron peristimulus time histogram (PSTH) of model and population dynamics obtained via various dimensionality reduction techniques (PCA, dPCA and jPCA) are in good to qualitative agreement with real MC data. To quantify the similarity, we applied CCA and Procrustes analysis to the projections of the model and neural data and found high correlation and consistency. Thus, our model strongly resembles the motor cortical dynamics, and make our analysis on the roles of internal dynamics and proprioceptive feedback convincing. We attribute the success of simulation to the advantage of ISN that is not trained for a particular movement, but contained a rich ensemble of quasi-oscillatory patterns that could be flexibly combined for the desired movement (Hennequin et al., 2014; Stroud et al., 2018). ISN aligns with the dynamical systems perspective that the MC generates a set of basic patterns for a large repertoire of movements. Moreover, unlike traditional RNN that optimized recurrent weights, we optimize the weights of initial conditions, whose number of parameters is much less than that of traditional RNN.

Second, internal dynamics predominantly govern cortical pattern generation during movement execution, consistent with the conclusion in Bachschmid-Romano et al. (2023). We find that disrupting internal dynamics greatly suppressed firing rates fluctuations and disrupted rotational dynamics. This may explain why many autonomous dynamical system models for the reach task achieve results similar to real data, as fast reaching movements are well pre-planned before initiation (Kao et al., 2021; Sussillo et al., 2015).

However, our findings diverge from a previous study (Kalidindi et al., 2021) in which sensory feedback contributed substantially to cortical dynamics. This difference may stem from the different methods of network analysis. First, the input during movement preparation only contains go cue signal and spatial position of the target in Kalidindi et al. (2021). This simple combination of feedforward inputs could not capture some remarkable features of preparation, such as various preparatory activity without causing movement and fast preparation(Kaufman et al., 2014; Ames et al., 2014). Theoretical work has provided strong evidence that feedforward input strategy need long time (at least 800 ms) to prepare for a movement (Kao et al., 2021). Thus, the insufficient preparation may led to bias toward the contribution of sensory feedback. Second, we employed a strategy of graded disruption (Sauerbrei et al., 2020) to dissect the contribution of proprioceptive feedback and internal dynamics. It could be rigid to infer from the amplitudes of currents generated from proprioceptive and internal dynamics source, since inputs positioned along the null-dimensions generate no output responses (Kao and Hennequin, 2019). Stavisky et al. (2017) showed that feedback-related motor cortical activity was isolated in null-dimensions that did not affect movement. Third, (Kalidindi et al., 2021) it may be inadequate to prove that network resembles motor cortical dynamics merely by the observation rotational dynamics. Rotational dynamics in the MC is widely observed during various movements, including reaching (Churchland et al., 2012), cycling (Russo et al., 2018), maintaining posture (Kalidindi et al., 2021), and even speaking (Stavisky et al., 2019). Therefore, rotational dynamics is probably a fundamental feature of motor cortical activity, but it may not evaluate a model sufficiently. There is a need for dependable evaluation index of network simulation.

Third, proprioceptive feedback control movement precision. A recent study in the fly shows that motor neurons that control head movement interact with proprioceptive feedback, suggesting that the brain controls movements by a proprioceptive-motor loop (Gorko et al., 2024). In this work, although proprioceptive feedback plays a modulatory role in neural population response compared to the internal dynamics, it significantly influenced behavior. We observed that disrupting proprioceptive feedback led to continuous, unceasing movement towards the target. A study found that the temporal offset in visual feedback extended deceleration duration (McKenna et al., 2017); proprioceptive feedback in our model may have similar effect. Moreover, the incorporation of sensory feedback in brain-machine interfaces has been shown to enable more efficient robotic arm control (Flesher et al., 2021; Suminski et al., 2010).

Furthermore, proprioceptive feedback enhances the network's robustness. After perturbing the initial conditions with different strategies, the network with proprioceptive feedback still reached the target with only a small deviation, especially compared to the autonomous model, which was sensitive to small differences in initial conditions. Tolerance to the variably of initial conditions is critical in any biologically network, as sensory and motor noise is present in nervous system and different initial conditions can lead to qualitatively similar movements (Churchland et al., 2006). Proprioceptive feedback tames the sensitivity to initial conditions at movement onset.

Addtionally, the sensory estimation network in our study is an abstract somatosensory system, including cuneate nucleus, ventroposterior nucleus of the thalamus, and somatosensory cortex (Lutz and Bensmaia, 2021). It is a task-driven model that predicts the kinematics (position and velocity) of the limb, better than data-driven model in predicting neural dynamics of proprioception (Vargas et al., 2024). Different from Chowdhury et al. (2020) that predicts joint kinematics, the sensory estimation network predicts hand kinematics and muscle force. First, area 2 of primary somatosensory cortex encodes kinematics of the whole arm (Chowdhury et al., 2020; Vargas et al., 2024). The whole-arm model (encoding the state of hand and joints) and hand-force model (encoding the state of hand and force) (Chowdhury et al., 2020) capture the features of neural activity comparably. Second, muscle force defined in our model and force defined in Chowdhury et al. (2020) are computed differently. Third, we found the MC network receiving the combination of hand state and muscle force is more similar to real data than the network receiving the combination of hand and joints states A7.

In conclusion, our model offers a computational framework to understand the interplay between cortical internal dynamics and proprioceptive feedback during movement execution. Nevertheless, there are some limitations in our model. First, the simulation of reaction period is oversimplified in our work. We assume that sensory feedback has a limited effect, but internal dynamics and stereotyped condition-independent signal shape the population response. Second, subjects use a flexible strategy that combines visual and proprioceptive feedback during reaching (Apker et al., 2011; Sober and Sabes, 2005), our model excluded visual feedback. Finally, our model need to be extended to more realistic and complex motor tasks to further investigate the contribution of proprioceptive feedback in movement execution.

Acknowledgements

This work was funded by the STI 2030—Major Projects (2022ZD0208604), and the National Natural Science Foundation of China (62176151 and 61773259). We are grateful to Guillaume Hennequin and Ta-Chu Kao for modeling instructions; to Juan Gallego and Matthew Perich for sharing the monkey data, and to Jieji Ren and Di Zhu for discussions.

Declaration of interest

The authors declare no competing interests.

Data and code availability

The monkey datasets have been deposited on Dryad. The code will be available on request.

References

Afshar, A., Santhanam, G., Byron, M.Y., Ryu, S.I., Sahani, M., Shenoy, K.V., 2011. Single-trial neural correlates of arm movement preparation. Neuron 71, 555–564.

Ames, K.C., Ryu, S.I., Shenoy, K.V., 2014. Neural dynamics of reaching following incorrect or absent motor preparation. Neuron 81, 438–451.

Apker, G., Karimi, C., Buneo, C., 2011. Contributions of vision and proprioception to arm movement planning in the vertical plane. Neuroscience letters 503, 186–190.

Bachschmid-Romano, L., Hatsopoulos, N.G., Brunel, N., 2023. Interplay between external inputs and recurrent dynamics during movement preparation and execution in a network model of motor cortex. Elife 12, e77690.

Bakken, T.E., Jorstad, N.L., Hu, Q., Lake, B.B., Tian, W., Kalmbach, B.E., Crow, M., Hodge, R.D., Krienen, F.M., Sorensen, S.A., et al., 2021. Comparative cellular analysis of motor cortex in human, marmoset and mouse. Nature 598, 111–119.

Brendel, W., Romo, R., Machens, C.K., 2011. Demixed principal component analysis. Advances in neural information processing systems 24.

Chen, A., Sun, Y., Lei, Y., Li, C., Liao, S., Meng, J., Bai, Y., Liu, Z., Liang, Z., Zhu, Z., et al., 2023. Single-cell spatial transcriptome reveals cell-type organization in the macaque cortex. Cell 186, 3726–3743.

Chowdhury, R.H., Glaser, J.I., Miller, L.E., 2020. Area 2 of primary somatosensory cortex encodes kinematics of the whole arm. Elife 9, e48198.

Chung, J., Gulcehre, C., Cho, K., Bengio, Y., 2014. Empirical evaluation of gated recurrent neural networks on sequence modeling. arXiv preprint arXiv:1412.3555 .

Churchland, M.M., Byron, M.Y., Ryu, S.I., Santhanam, G., Shenoy, K.V., 2006. Neural variability in premotor cortex provides a signature of motor preparation. Journal of Neuroscience 26, 3697–3712.

Churchland, M.M., Cunningham, J.P., Kaufman, M.T., Foster, J.D., Nuyujukian, P., Ryu, S.I., Shenoy, K.V., 2012. Neural population dynamics during reaching. Nature 487, 51–56.

Churchland, M.M., Cunningham, J.P., Kaufman, M.T., Ryu, S.I., Shenoy, K.V., 2010. Cortical preparatory activity: representation of movement or first cog in a dynamical machine? Neuron 68, 387–400.

Crevecoeur, F., Munoz, D.P., Scott, S.H., 2016. Dynamic multisensory integration: somatosensory speed trumps visual accuracy during feedback control. Journal of Neuroscience 36, 8598–8611.

Cunningham, J.P., Ghahramani, Z., 2015. Linear dimensionality reduction: Survey, insights, and generalizations. The Journal of Machine Learning Research 16, 2859–2900.

Eskikand, P.Z., Soto-Breceda, A., Cook, M.J., Burkitt, A.N., Grayden, D.B., 2023. Inhibitory stabilized network behaviour in a balanced neural mass model of a cortical column. Neural Networks 166, 296–312.

Even-Chen, N., Sheffer, B., Vyas, S., Ryu, S.I., Shenoy, K.V., 2019. Structure and variability of delay activity in premotor cortex. PLoS computational biology 15, e1006808.

Flesher, S.N., Downey, J.E., Weiss, J.M., Hughes, C.L., Herrera, A.J., Tyler-Kabara, E.C., Boninger, M.L., Collinger, J.L., Gaunt, R.A., 2021. A brain-computer interface that evokes tactile sensations improves robotic arm control. Science 372, 831–836.

Gallego, J.A., Perich, M.G., Chowdhury, R.H., Solla, S.A., Miller, L.E., 2020. Long-term stability of cortical population dynamics underlying consistent behavior. Nature neuroscience 23, 260–270.

Gallego-Carracedo, C., Perich, M.G., Chowdhury, R.H., Miller, L.E., Gallego, J.Á., 2022. Local field potentials reflect cortical population dynamics in a region-specific and frequency-dependent manner. Elife 11, e73155.

Georgopoulos, A.P., Kalaska, J.F., Caminiti, R., Massey, J.T., 1982. On the relations between the direction of two-dimensional arm movements and cell discharge in primate motor cortex. Journal of Neuroscience 2, 1527–1537.

Gorko, B., Siwanowicz, I., Close, K., Christoforou, C., Hibbard, K.L., Kabra, M., Lee, A., Park, J.Y., Li, S.Y., Chen, A.B., et al., 2024. Motor neurons generate pose-targeted movements via proprioceptive sculpting. Nature , 1–8.

Hennequin, G., Vogels, T.P., Gerstner, W., 2012a. Non-normal amplification in random balanced neuronal networks. Physical Review E 86, 011909.

Hennequin, G., Vogels, T.P., Gerstner, W., 2012b. Non-normal amplification in random balanced neuronal networks. Physical Review E 86, 011909.

Hennequin, G., Vogels, T.P., Gerstner, W., 2014. Optimal control of transient dynamics in balanced networks supports generation of complex movements. Neuron 82, 1394–1406.

Herter, T.M., Korbel, T., Scott, S.H., 2009. Comparison of neural responses in primary motor cortex to transient and continuous loads during posture. Journal of neurophysiology 101, 150–163.

Inoue, Y., Mao, H., Suway, S.B., Orellana, J., Schwartz, A.B., 2018. Decoding arm speed during reaching. Nature communications 9, 5243.

Kalaska, J.F., 2019. Emerging ideas and tools to study the emergent properties of the cortical neural circuits for voluntary motor control in non-human primates. F1000Research 8.

Kalidindi, H.T., Cross, K.P., Lillicrap, T.P., Omrani, M., Falotico, E., Sabes, P.N., Scott, S.H., 2021. Rotational dynamics in motor cortex are consistent with a feedback controller. Elife 10, e67256.

Kao, T.C., Hennequin, G., 2019. Neuroscience out of control: control-theoretic perspectives on neural circuit dynamics. Current opinion in neurobiology 58, 122–129.

Kao, T.C., Sadabadi, M.S., Hennequin, G., 2021. Optimal anticipatory control as a theory of motor preparation: A thalamo-cortical circuit model. Neuron 109, 1567–1581.

Kaufman, M.T., Churchland, M.M., Ryu, S.I., Shenoy, K.V., 2014. Cortical activity in the null space: permitting preparation without movement. Nature neuroscience 17, 440–448.

Kaufman, M.T., Seely, J.S., Sussillo, D., Ryu, S.I., Shenoy, K.V., Churchland, M.M., 2016. The largest response component in the motor cortex reflects movement timing but not movement type. eneuro 3.

Kobak, D., Brendel, W., Constantinidis, C., Feierstein, C.E., Kepecs, A., Mainen, Z.F., Qi, X.L., Romo, R., Uchida, N., Machens, C.K., 2016. Demixed principal component analysis of neural population data. elife 5, e10989.

Kumar, G., Ma, C.H.E., 2023. Toward a cerebello-thalamo-cortical computational model of spinocerebellar ataxia. Neural Networks 162, 541–556.

Lillicrap, T.P., Scott, S.H., 2013. Preference distributions of primary motor cortex neurons reflect control solutions optimized for limb biomechanics. Neuron 77, 168–179.

Logiaco, L., Abbott, L., Escola, S., 2021. Thalamic control of cortical dynamics in a model of flexible motor sequencing. Cell reports 35.

Lutz, O.J., Bensmaia, S.J., 2021. Proprioceptive representations of the hand in somatosensory cortex. Current Opinion in Physiology 21, 9–16.

McKenna, E., Bray, L.C.J., Zhou, W., Joiner, W.M., 2017. The absence or temporal offset of visual feedback does not influence adaptation to novel movement dynamics. Journal of Neurophysiology 118, 2483–2498.

Michaels, J.A., Dann, B., Scherberger, H., 2016. Neural population dynamics during reaching are better explained by a dynamical system than representational tuning. PLoS computational biology 12, e1005175.

Omrani, M., Kaufman, M.T., Hatsopoulos, N.G., Cheney, P.D., 2017. Perspectives on classical controversies about the motor cortex. Journal of neurophysiology 118, 1828–1848.

Pandarinath, C., O'Shea, D.J., Collins, J., Jozefowicz, R., Stavisky, S.D., Kao, J.C., Trautmann, E.M., Kaufman, M.T., Ryu, S.I., Hochberg, L.R., et al., 2018. Inferring single-trial neural population dynamics using sequential auto-encoders. Nature methods 15, 805–815.

Perich, M., Conti, S., Badi, M., Bogaard, A., Barra, B., Wurth, S., Bloch, J., Courtine, G., Micera, S., Capogrosso, M., et al., 2020. Motor cortical dynamics are shaped by multiple distinct subspaces during naturalistic behavior (p. 2020.07. 30.228767).

Proske, U., Gandevia, S.C., 2012. The proprioceptive senses: their roles in signaling body shape, body position and movement, and muscle force. Physiological reviews .

Pruszynski, J.A., Omrani, M., Scott, S.H., 2014. Goal-dependent modulation of fast feedback responses in primary motor cortex. Journal of Neuroscience 34, 4608–4617.

Russo, A.A., Bittner, S.R., Perkins, S.M., Seely, J.S., London, B.M., Lara, A.H., Miri, A., Marshall, N.J., Kohn, A., Jessell, T.M., et al., 2018. Motor cortex embeds muscle-like commands in an untangled population response. Neuron 97, 953–966.

Safaie, M., Chang, J.C., Park, J., Miller, L.E., Dudman, J.T., Perich, M.G., Gallego, J.A., 2023. Preserved neural dynamics across animals performing similar behaviour. Nature 623, 765–771.

Sainburg, R.L., Ghilardi, M.F., Poizner, H., Ghez, C., 1995. Control of limb dynamics in normal subjects and patients without proprioception. Journal of neurophysiology 73, 820–835.

Sauerbrei, B.A., Guo, J.Z., Cohen, J.D., Mischiati, M., Guo, W., Kabra, M., Verma, N., Mensh, B., Branson, K., Hantman, A.W., 2020. Cortical pattern generation during dexterous movement is input-driven. Nature 577, 386–391.

Scott, S.H., 2004. Optimal feedback control and the neural basis of volitional motor control. Nature Reviews Neuroscience 5, 532–545.

Sergio, L.E., Hamel-Pâquet, C., Kalaska, J.F., 2005. Motor cortex neural correlates of output kinematics and kinetics during isometric-force and arm-reaching tasks. Journal of neurophysiology 94, 2353–2378.

Shenoy, K.V., Sahani, M., Churchland, M.M., 2013. Cortical control of arm movements: a dynamical systems perspective. Annual review of neuroscience 36, 337–359.

Sober, S.J., Sabes, P.N., 2005. Flexible strategies for sensory integration during motor planning. Nature neuroscience 8, 490–497.

Stavisky, S.D., Kao, J.C., Ryu, S.I., Shenoy, K.V., 2017. Motor cortical visuomotor feedback activity is initially isolated from downstream targets in output-null neural state space dimensions. Neuron 95, 195–208.

Stavisky, S.D., Willett, F.R., Wilson, G.H., Murphy, B.A., Rezaii, P., Avansino, D.T., Memberg, W.D., Miller, J.P., Kirsch, R.F., Hochberg, L.R., et al., 2019. Neural ensemble dynamics in dorsal motor cortex during speech in people with paralysis. Elife 8, e46015.

Stroud, J.P., Porter, M.A., Hennequin, G., Vogels, T.P., 2018. Motor primitives in space and time via targeted gain modulation in cortical networks. Nature neuroscience 21, 1774–1783.

Suminski, A.J., Tkach, D.C., Fagg, A.H., Hatsopoulos, N.G., 2010. Incorporating feedback from multiple sensory modalities enhances brain–machine interface control. Journal of Neuroscience 30, 16777–16787.

Suresh, A.K., Goodman, J.M., Okorokova, E.V., Kaufman, M., Hatsopoulos, N.G., Bensmaia, S.J., 2020. Neural population dynamics in motor cortex are different for reach and grasp. Elife 9, e58848.

Sussillo, D., Churchland, M.M., Kaufman, M.T., Shenoy, K.V., 2015. A neural network that finds a naturalistic solution for the production of muscle activity. Nature neuroscience 18, 1025–1033.

Todorov, E., Jordan, M.I., 2002. Optimal feedback control as a theory of motor coordination. Nature neuroscience 5, 1226–1235.

Vargas, A.M., Bisi, A., Chiappa, A.S., Versteeg, C., Miller, L.E., Mathis, A., 2024. Task-driven neural network models predict neural dynamics of proprioception. Cell 187, 1745–1761.e19.

Vyas, S., Golub, M.D., Sussillo, D., Shenoy, K.V., 2020. Computation through neural population dynamics. Annual review of neuroscience 43, 249–275.

Yu, Y., Han, F., Wang, Q., 2022. Exploring phase–amplitude coupling from primary motor cortex-basal ganglia–thalamus network model. Neural Networks 153, 130–141.

Zimnik, A.J., Churchland, M.M., 2021. Independent generation of sequence elements by motor cortex. Nature neuroscience 24, 412–424.